



1 Global application of a regional frequency  
2 analysis on extreme sea levels  
3

4 Authors: Thomas P. Collings<sup>1</sup>, Niall D. Quinn<sup>1</sup>, Ivan D. Haigh<sup>1,2</sup>, Joshua Green<sup>1,2</sup>, Izzy Probyn<sup>1</sup>, Hamish  
5 Wilkinson<sup>1</sup>, Sanne Muis<sup>3,4</sup>, William V. Sweet<sup>5</sup>, Paul D. Bates<sup>1,6</sup>

6

7 Affiliations of Authors:

8 1. Fathom, Floor 2, Clifton Heights, Clifton, Bristol, UK. BS8 1EJ

9 2. School of Ocean and Earth Science, University of Southampton, National Oceanography Centre,  
10 European Way, Southampton SO14 3ZH

11 3. Deltares, Delft, Netherlands

12 4. Institute for Environmental Studies (IVM), Vrije Universiteit Amsterdam, Amsterdam, Netherlands

13 5. National Oceanic and Atmospheric Administration, National Ocean Service, Silver Spring, MD,  
14 United States

15 6. School of Geographical Sciences, University of Bristol, Bristol, UK

16 Correspondence to: [t.collings@fathom.global](mailto:t.collings@fathom.global)

17

18

19

20

21

22

23

24

25



## 26 Abstract

27 Coastal regions face increasing threats from rising sea levels and extreme weather events,  
28 highlighting the urgent need for accurate assessments of coastal flood risk. This study  
29 presents a novel approach to estimating global Extreme Sea Level (ESL) exceedance  
30 probabilities, using a Regional Frequency Analysis (RFA) approach. The research combines  
31 observed and modelled hindcast data to produce a high-resolution (~1 km) dataset of ESL  
32 exceedance probabilities, including wave setup, along the entire global coastline, excluding  
33 Antarctica.

34

35 The RFA approach offers several advantages over traditional methods, particularly in regions  
36 with limited observational data. It overcomes the challenge of short and incomplete  
37 observational records by substituting long historical records with a collection of shorter but  
38 spatially distributed records. This spatially distributed data not only retains the volume of  
39 information but also addresses the issue of sparse tide gauge coverage in less populated  
40 areas and developing nations. The RFA process is illustrated using Cyclone Yasi (2011) as a  
41 case study, demonstrating how the approach can significantly improve the characterisation  
42 of ESLs in regions prone to tropical cyclone activity.

43

44 In conclusion, this study provides a valuable resource for quantifying global coastal flood  
45 risk, offering an innovative methodology that can contribute to preparing for, and mitigating  
46 against, coastal flooding.

47

## 48 Plain language summary

49 Coastal areas are at risk of flooding from rising sea levels and extreme weather events. This study  
50 uses a new way to figure out how likely coastal flooding is around the world. The method uses data  
51 from observations and computer models to create a detailed map of where these floods might  
52 happen at the coast. The approach can predict flooding in areas where there is little or no data. The  
53 results can be used to help get ready for and prevent this type of flooding.

54

55



56 **1. Introduction**

57 Flooding provides one of the greatest threats to coastal communities globally, causing  
58 devastating impacts to affected regions. Notable events which have caused significant  
59 coastal flooding in recent years include: Cyclone Amphan (2020), which struck the Bay of  
60 Bengal producing a storm surge of up to 4.6m along the coast of Western Bengal, killing 84  
61 people, and causing total losses over 13 billion USD (India Meteorological Department,  
62 2020, Kumar *et al.*, 2021); Hurricane Harvey (2017), the second most costly hurricane to hit  
63 the US after Katrina (2005), which impacted 13 million people, hitting the state of Texas  
64 with a maximum storm surge of 3.8m (Amadeo, 2019); and Typhoon Jebi (2018), driving  
65 storm surges of over 3m in Osaka Bay, Japan, combined with wave action which led to  
66 flooding exceeding 5m above mean sea level (Mori *et al.*, 2019). Approximately 10% of the  
67 world's population (768 million people) live below 10m above mean sea level (Nicholls *et*  
68 *al.*, 2021). Coastal flooding is expected to increase dramatically into the future,  
69 predominantly caused by sea-level rise (Taherkhani *et al.*, 2020), and compounded by  
70 continued growth and development in coastal populations (Neumann *et al.*, 2015).  
71 Therefore, continuing to improve the understanding of coastal flooding is vital.

72 Coastal floods are driven by extreme sea levels, which arise as combinations of: (1)  
73 astronomical tides; (2) storm surges (driven by tropical and extra-tropical cyclones) and  
74 associated seiches; (3) waves, especially setup and runup; and (4) relative mean sea level  
75 changes (including sea-level rise and vertical land movement). Risk assessments of coastal  
76 flooding require high-quality and high-resolution flood hazard data, typically in the form of  
77 flood inundation maps. Inundation maps are usually derived from hydraulic models, which  
78 use high resolution extreme sea level (ESL) exceedance probabilities as a key input (e.g.,  
79 Bates *et al.*, 2021; Mitchell *et al.*, 2022). The development of coastal inundation maps is  
80 reliant on coastal boundary conditions points that vary in resolution depending on  
81 application. Previous studies such (e.g., Barnard *et al.*, 2019) have used 100m resolution at  
82 local scales, while regional studies (e.g., Bates *et al.*, 2021, Environment Agency, 2018) have  
83 employed resolutions between 500m and 2km.

84 Traditional methods for computing ESL exceedance probabilities involve extreme value  
85 analysis of measurements from individual tide gauges or wave buoys. However, long,  
86 complete records spanning numerous decades are necessary to obtain robust estimates of



87 ESL return levels (Coles, 2001). The Global Extreme Sea Level Analysis (GESLA-3) database  
88 provides sea level records for over 5,000 tide gauge stations (Haigh *et al.*, 2021), but these  
89 tide gauges still cover only a small fraction of the world's coastlines. Wave buoys are even  
90 more sparse, largely restricted to the Northern Hemisphere and long historical records are  
91 marred by discontinuities (Timmermans *et al.*, 2020). Even in areas with relatively high tide  
92 gauge or wave buoy density, there are still large expanses of coastline which remain  
93 ungauged. While rare extreme weather events (such as intense tropical cyclones) are often  
94 many hundreds of kilometres in size, the precise impact of the corresponding ESL can often  
95 be highly localised (Irish *et al.*, 2008), meaning the peak surge occurs in an ungauged  
96 location. The particular locale of peak surge for an event is determined by storm  
97 characteristics, local bathymetry and coastal geography, amongst other factors (Shaji *et al.*,  
98 2014). Therefore, relying on past observation-based analyses of ESL exceedance  
99 probabilities to characterise return levels across a region will likely lead to the under  
100 representation of rare extreme events. Finally, another limitation is that many previous  
101 analyses of ESL exceedance probabilities consider the still water level component (i.e., tide  
102 plus storm surge) separately from the wave set up and run up (Haigh *et al.*, 2016, Muis *et*  
103 *al.*, 2016, Ramakrishnan *et al.*, 2022).

104 One solution to overcome sparse datasets is to use ESL hindcasts created by state-of-the-art  
105 models. These include regional (e.g., (Andrée *et al.*, 2021, Siah sarani *et al.*, 2021, Tanim &  
106 Akter, 2019) or global tide-surge (such as Deltares' Global Tide Surge Model v3.0 (hereafter  
107 referred to as GTSM; Muis *et al.*, 2020) or wave models (e.g., Liang *et al.*, 2019). These are  
108 used to fill the spatial and temporal gaps in the observation records via historical reanalysis  
109 simulation. However, their ability to accurately capture extreme events is hampered by the  
110 atmospheric forcing data that is used to drive the models, as reanalysis products like ERA5  
111 (Hersbach *et al.*, 2020) commonly contain biases in representing meteorological extremes  
112 such as tropical cyclones (Slocum *et al.*, 2022), leading to an underestimation of event  
113 intensity. Furthermore, the time period captured in reanalysis products is not adequate to  
114 represent the characteristics (e.g., frequencies) of particularly rare events such as intense  
115 tropical cyclones. To overcome this limitation, some studies have used synthetic event  
116 datasets representing tropical cyclone activity over many thousands of years (e.g., Haigh *et*  
117 *al.*, 2014; Dullaart *et al.*, 2021), however this approach is computationally expensive.



118 An alternative and less computationally demanding solution that helps address some of the  
119 problems inherent in estimating ESLs around the world's coastlines from the observational  
120 record, is regional frequency analysis (RFA). The RFA methodology was originally developed  
121 to estimate streamflow within a hydrological context (e.g., Hosking and Wallis, 1997), but  
122 has since been used in many applications requiring extreme value analysis of meteorological  
123 parameters including coastal storm surge (e.g., Bardet *et al.*, 2011; Weiss and Bernardara,  
124 2013; Arns *et al.*, 2015) and extreme ocean waves (e.g., Campos *et al.*, 2019, Lucas *et al.*,  
125 2017, Vanem, 2017). The principle of an RFA is founded on the basis that a homogenous  
126 region can be identified, throughout which similar meteorological forcings and resultant  
127 storm surge or wave events could occur, even if the extreme events have not been seen in  
128 part of that region in the historical record (Hosking and Wallis, 1997). RFA has been used on  
129 a regional scale to produce coastal ESL exceedance probabilities including: France  
130 (Andreevsky *et al.*, 2020, Hamdi *et al.*, 2016); the US coastline (Sweet *et al.*, 2022); Northern  
131 Europe (Frau *et al.*, 2018); US coastal military sites (Hall *et al.*, 2016); and the Pacific Basin  
132 (Sweet *et al.*, 2020). However, an RFA approach has not (to our knowledge) been applied  
133 globally.

134 The overall aim of this paper is to, for the first time, apply an RFA approach to estimate ESL  
135 exceedance probabilities, including wave setup, along the entire global coastline. These  
136 exceedance probabilities aim to better characterise ESLs driven by rare, extreme events,  
137 such as those from tropical cyclones, which are poorly represented in the historical record.  
138 Uniquely, this study uses both measured and hindcast datasets; includes tides, storm surges,  
139 and wave setup; and calculates exceedance probabilities at high resolution (1 km) globally.  
140 The specific objectives of this paper are to:

- 141 (1) develop and apply the RFA globally (excluding Antarctica), utilising both  
142 observational tide gauge, and modelled hindcast sea level and wave records;
- 143 (2) illustrate how the RFA methodology improves the representation of rare extreme  
144 events in the ESL exceedance probabilities using cyclone Yasi, which impacted the  
145 Australian coastline in 2011, as a case study;
- 146 (3) validate the RFA against exceedance probabilities estimated from the GESLA-3 global  
147 tide gauge database; and



148 (4) Finally, quantify how much the RFA improves the estimation of ESL exceedance  
149 probabilities when compared to single site analysis, using hindcast datasets (Muis *et*  
150 *al.*, 2020 and Dullaart *et al.*, 2021).

151 This paper is laid out as follows: The datasets used are described in Section 2. The  
152 methodology is detailed in Section 3, addressing objective 1. Results and validation are  
153 described in Section 4, addressing objectives 2, 3, and 4. A discussion of the key findings and  
154 conclusions are then given in Sections 5 and 6, respectively.

155

## 156 2. Data

157 We use seven primary sources of data in this study, namely: (1) still sea-level observations  
158 contained in the GESLA-3 tide gauge dataset; (2) global still sea-level simulations from the  
159 GTSM hindcast based on the ERA5 climate reanalysis; (3) tidal predictions from the FES2014  
160 finite element hydrodynamic model; (4) significant wave heights derived from the ERA5  
161 climate reanalysis; (5) mean dynamic topography from HYBRID-CNES-CLS18-CMEMS2020;  
162 (6) Copernicus DEM to create a global coastline dataset; and (7) the COAST-RP dataset from  
163 Dullaart *et al.*, (2021) to validate the RFA methodology. These seven datasets are described  
164 in turn below.

165 Still sea level records are assembled from the GESLA-3 (Global Extreme Sea Level Analysis)  
166 tide gauge dataset version 3 (Caldwell *et al.*, 2015, Haigh *et al.*, 2021). The GESLA-3 dataset  
167 includes high-frequency water level time series from over 5,000 tide gauges around the  
168 globe, collated from 36 international and national providers. Data providers have differing  
169 methods of quality control, however each record was visually assessed by the authors of the  
170 GESLA-3 dataset and graded as either: (i) no obvious issues; (ii) possible datum issues; (iii)  
171 possible quality control issues; or (iv) possible datum and quality control issues. Only  
172 records with no obvious issues were used in this study.

173 As discussed in Section 3, the hindcast, GTSM-ERA5 is used in all areas which are not  
174 covered by tide gauge observations. GTSM is a depth-averaged hydrodynamic model built  
175 using the DELFT-3D hydrodynamic model, which makes use of an unstructured, global,  
176 flexible mesh with no open boundaries (Muis *et al.*, 2020). The model has a coastal



177 resolution of 2.5km (1.25km in Europe), and a deep ocean resolution of 25km. The GTSM-  
178 ERA5 dataset spans the period 1979-2018, and is developed by forcing GTSM with hourly  
179 fields of ERA5 10-metre wind speed and atmospheric pressure (Hersbach *et al.*, 2020).  
180 GTSM-ERA5 has a 10-minute temporal resolution and provides a timeseries at locations  
181 approximately every 50km along the coastline (10km in Europe). Validation carried out by  
182 Muis *et al.* (2020) shows that the dataset performs well against observations of annual  
183 maximum water level, exhibiting a mean bias of -0.04 m and a mean absolute percentage  
184 error of 14%.

185 We use the FES2014 tidal database to generate tidal timeseries at GTSM-ERA5 locations and  
186 RFA output locations. The RFA output resolution is much higher than the output resolution  
187 of GTSM-ERA5, which is why FES2014 is used instead. FES2014 is a finite element  
188 hydrodynamic model which combines data assimilation from satellite altimetry and tide  
189 gauges (Lyard *et al.*, 2021). The model solves the barotropic tidal equations, as well as the  
190 effects from self-attraction and loading. The gridded resolution of the output is  $1/16^\circ$ . The  
191 model was extensively validated against tide gauges, satellite altimeter observations, and  
192 alternative global tide models by Lyard *et al.* (2021) and was found to have an improved  
193 variance reduction in nearly all areas, especially in shallow water regions. The Python  
194 package distributed with the FES2014 data (<https://github.com/CNES/aviso-fes>) was used to  
195 simulate tidal timeseries.

196 To calculate wave set up we use significant wave heights ( $H_s$ ) from the ERA5 reanalysis  
197 (Hersbach *et al.*, 2020), covering the period 1979 to 2020. The spatial resolution of the ERA5  
198 wave model output is  $0.5^\circ \times 0.5^\circ$ , and the temporal resolution is hourly. Independent  
199 validation of hourly  $H_s$  performed by Wang & Wang (2022) finds little bias in the dataset (-  
200 0.058 m), however the authors go on to conclude that  $H_s$  of extreme waves tends to be  
201 underestimated (by 7.7% in the 95% percentile), a conclusion supported by Fanti *et al.*  
202 (2023).

203 We use mean dynamic topography (MDT) to convert water levels from mean sea level as  
204 measured by tide gauges to mean sea level as referenced by a geoid, for use in subsequent  
205 future studies involving inundation assessments using hydraulic modelling. MDT describes  
206 the change in sea surface height due to the effects of the winds and currents in the ocean.  
207 Digital elevation models (DEMs), a key input to hydraulic models, typically use a geoid as a



208 vertical datum. A geoid is an equipotential surface of mean sea level under the sole effect of  
209 gravity, in the absence of land masses, currents and tides (Bingham & Haines, 2006). To  
210 convert water levels from tide gauge mean sea level to the geoid mean sea level, the  
211 HYBRID-CNES-CLS18-CMEMS2020 MDT dataset is used (Mulet *et al.*, 2021). Errors  
212 associated with this dataset are largely caused by the input satellite altimetry data and can  
213 be up to 10 cm in some areas. The MDT at the shoreline is illustrated in the Appendix Fig.  
214 A1.

215 The Copernicus 30m DEM (European Space Agency, 2021) is used to create a high-resolution  
216 global coastline. This is used to define the RFA output points at approximately 1 km intervals  
217 along the global coastline (excluding Antarctica), resulting in over 3.4 million points.

218 Finally, in addition to GTSM-ERA5, we use the COAST-RP dataset from Dullaart *et al.* (2021)  
219 to validate the RFA methodology. COAST-RP uses the same hydraulic modelling framework  
220 as GTSM-ERA5 but simulates extra-tropical and tropical surge events separately using  
221 different forcing data. In areas prone to tropical cyclone activity, synthetic tropical cyclones  
222 representing 10,000 years under current climate conditions are used from the STORM  
223 dataset (Bloemendaal *et al.*, 2020). These synthetic tropical cyclone model runs have been  
224 validated against observed IBTrACS-forced model runs, and found to show differences in  
225 ESLs at the 1 in 25 year return level of less than 0.1 m at 67% of the output locations in  
226 tropical cyclone prone areas (Dullaart *et al.*, 2021). In extra-tropical regions, a 38-year  
227 timeseries of ERA5 data is used (Hersbach *et al.*, 2020). The surge levels from each set of  
228 simulations are probabilistically combined with tides to result in a global database of  
229 dynamically modelled storm-tides.

230

### 231 3. Methods

232 The first objective of this study is to develop and apply an RFA approach globally,  
233 encompassing still water levels and wave set up. In Section 3.1 we describe the methods  
234 used to process the data used in this study. In Section 3.2 we layout the global application of  
235 the RFA approach using observational and modelled data. The methods used to validate the  
236 results are explained in Section 3.3.

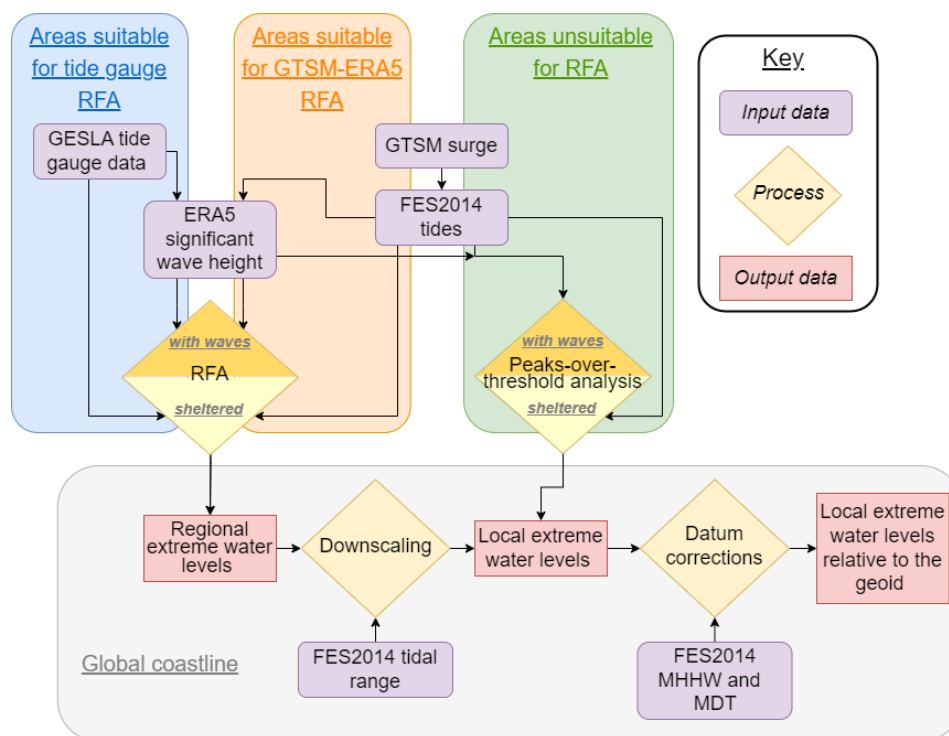




237 An overview of our methodology is illustrated in Fig. 1. This study broadly follows the  
238 methodology of Sweet *et al.* (2022) and applies an RFA to both tide gauge and GTSM-ERA5  
239 records. As such, the terms ‘water level record’ and ‘record location’ are used to describe  
240 both tide gauge records and GTSM-ERA5 data. The method can be summarised in five key  
241 steps: (i) collation and pre-processing of tide gauge, GTSM-ERA5, FES2014, and ERA5 Hs  
242 data; (ii) spatial discretisation of water level records into regions; (iii) application of the RFA  
243 to regional water level records (in areas unsuitable for an RFA, a peaks-over-threshold  
244 analysis of individual GTSM-ERA5 water level records is used); (iv) conversion (downscaling)  
245 of RFA exceedance levels to local exceedance levels at the output coastline points, using  
246 FES2014 tidal range (in areas unsuitable for an RFA, nearest-neighbour interpolation is  
247 used to assign local exceedance levels); and (v) correction of datums to convert water levels  
248 to geoid mean sea level, using FES2014 mean higher high water and global MDT (HYBRID-  
249 CNES-CLS18-CMEMS2020). These steps are described in detail below.



250



251

252 *Figure 1: Schematic flow diagram detailing the data sources and processes involved in producing a global set of extreme*  
253 *water levels*

### 254 3.1 Data processing

255

256 The GESLA-3 dataset was filtered to sample appropriate input data by removing duplicates,  
257 gauges located in rivers (away from the coast), and gauges that fail quality control checks  
258 (such as suspected datum jumps). A total of 2,223 tide gauges with a mean record length of  
259 21.4 years were used in the RFA. The surge component of GTSM-ERA5 at each record  
260 location is isolated from the water level timeseries using a tideonly simulation and  
261 superimposed upon a tidal timeseries created with FES2014, as the FES2014 tidal elevations  
262 performed better than those of GTSM. Tidal timeseries were also computed at each of the  
263 coastline output locations for use in downscaling the regional outputs, and in the bias and  
264 datum corrections of the local ESL.



265 Wave setup is the static increase in water level attributed to residual energy remaining after  
266 a wave breaks (Dean & Walton, 2010), and therefore is only observed in areas exposed to  
267 direct wave action. In this study, wave setup is approximated as 20% significant wave height  
268 ( $H_s$ ) from the ERA5 reanalysis, following the recommendation from the review of numerous  
269 laboratory and field experiments (Dean & Walton, 2010) and previous related studies (Bates  
270 *et al.*, 2021, Vousdoukas *et al.*, 2016). Wave setup is interpolated to the nearest record  
271 location using a nearest-neighbour approach. To account for the lack of wave setup in  
272 sheltered areas (e.g., bays and estuaries), the global coastline is classified as either sheltered  
273 or exposed, and the final extreme water levels are drawn from an RFA that is processed with  
274 or without wave setup added in. To classify the coastline, each coastline point is evaluated  
275 to determine if it is exposed from a minimum  $22.5^\circ$  angle over a fetch of 50km. A total of 16  
276 equall angle transects are drawn, extending 50km from each coastline point. If two or more  
277 adjacent transects do not intersect with land, the coastline point is considered exposed.

278 To process the RFA with wave setup, daily maximum wave setup is added to the daily  
279 highest water levels. Where tide gauge records fall outside of the temporal range of the  
280 ERA5 data, a copula-based approach was used to fit a simple statistical model between daily  
281 peak water levels and daily max  $H_s$ , providing a prediction of the daily max  $H_s$ . The RFA is  
282 then executed as described below. Tide gauges are assumed to be located in sheltered  
283 regions, such as bays and estuaries, thus tide gauge records are not impacted by wave  
284 setup.

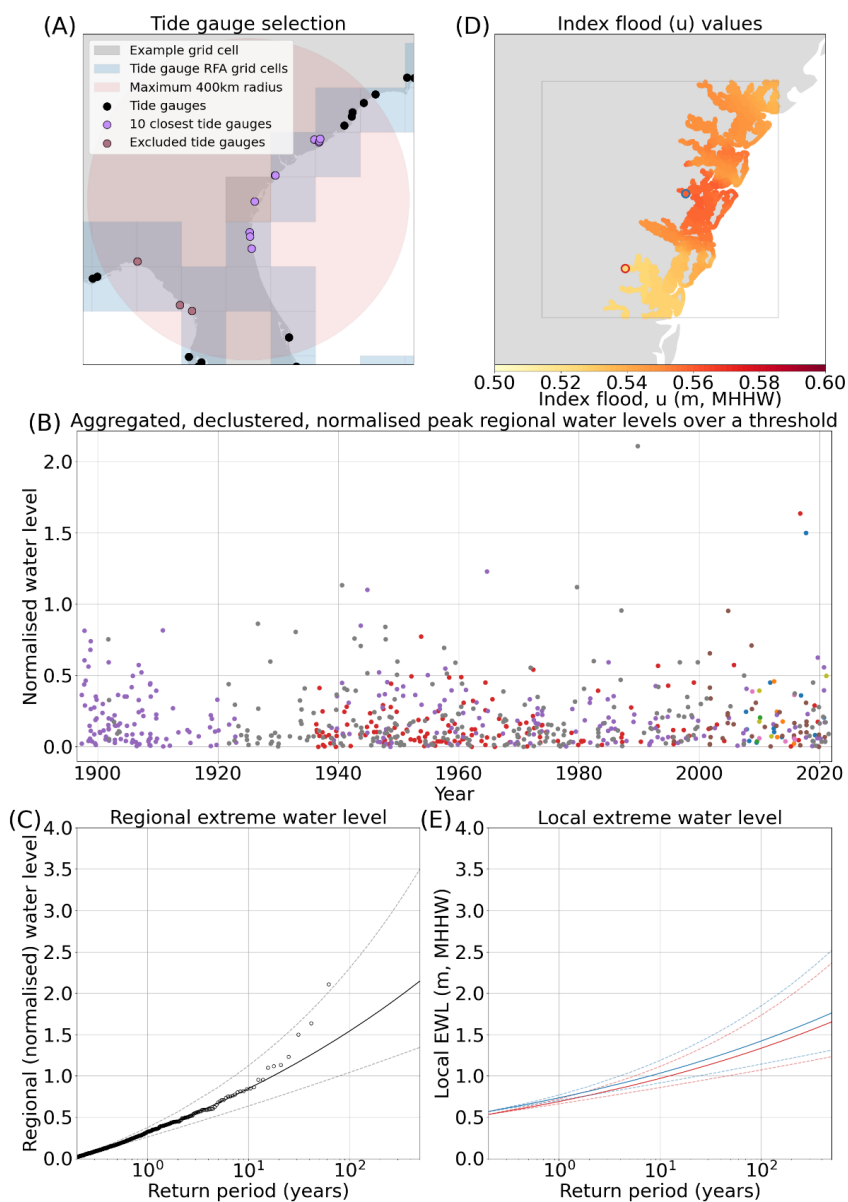
### 285 3.2 RFA

286

287 Water level records are spatially clustered to form a potential pool from which regional  
288 exceedance levels can be characterised. To do this, the global coastline is divided into  $1^\circ$  by  
289  $1^\circ$  grid cells, which are used as the regions to apply the outputs for each RFA. All record  
290 locations within a 400km radius (same as Hall *et al.* (2016) and Sweet *et al.* (2022)) of the  
291 grid cell centroid that have at least 10 consecutive years of good (>90% completeness) data  
292 are identified (minimum of 3 water level records, maximum of 10). This step is illustrated in  
293 Fig. 2A. Record locations which are geographically within range, but are separated by a large  
294 expanse of land, and thus likely forced by different storm patterns are removed from the  
295 record location selection. To achieve this, a line is drawn between the grid cell centroid and



296 each record location. The land intersected by the line is divided, and the areas of land on  
297 either side of the line are summed. A ratio of the length of the line to the area of land  
298 segmented by the line is then calculated. A threshold of 100 was empirically evaluated using  
299 expert judgement based on a number of test cases, above which records are removed from  
300 the grid cell analysis. This approach ensures that, for example, record locations located on  
301 the east coast of Florida (e.g., Mayport) are not grouped with those on the west coast (e.g.,  
302 Cedar Key) when characterising regional growth curves, despite the relatively short straight-  
303 line distance between them. Fig. 2A exemplifies three tide gauges which have been  
304 excluded from possible selection despite lying within a 400km radius to the grid cell centroid  
305 as the land that separates them is considerably large when compared to the distance. This  
306 spatial discretisation of regions results in a total of 836 tide gauge records and 18628 GTSM-  
307 ERA5 records for use in the application of the RFA.

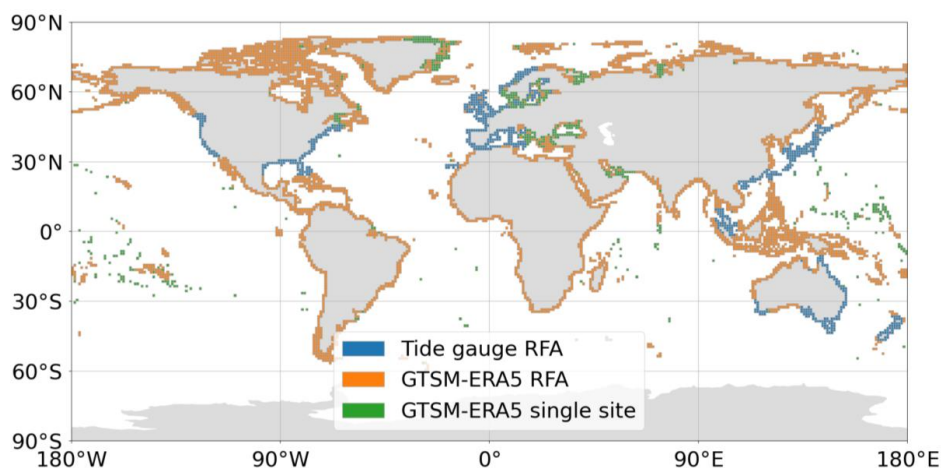


308

309 *Figure 2: Illustrating a selection of the steps through the RFA. (A) The 1° by 1° grid cells along the East Coast of the US,*  
 310 *along with the locations of the tide gauges, and the tide gauges selected for the RFA of the example grid cell. The tide*  
 311 *gauges excluded from possible selection by the distance/land area ratio are also indicated. (B) The aggregated, declustered,*  
 312 *normalised peak regional water levels over a threshold for each of the tide gauges used in the example grid cell. The colours*  
 313 *indicate peak water levels from the individual tide gauges in the region. (C) The regional extreme water levels, ascertained*  
 314 *by fitting a Generalised Pareto distribution to the data displayed in panel (B). (D) The index flood values of the example grid*  
 315 *cell, found by linearly interpolating the u value from the two closest tide gauges, and scaling by tidal range. The locations of*  
 316 *two coastline points used to produce local extreme water levels in panel E are also highlighted. (E) The local extreme water*  
 317 *level at two shoreline points inside the example grid cell, each with different index flood values as indicated in panel D.*



318 The RFA is preferentially applied to tide gauges in areas where the gauge density is sufficient  
319 (minimum 3 gauges within a 400km radius, same as Hall *et al.* (2016) and Sweet *et al.*  
320 (2022)). Outside of these areas, the RFA is implemented using data from GTSM-ERA5. In  
321 some regions, the density of record locations from GTSM-ERA5 is also too low for the RFA to  
322 function, in which case the ESL exceedance probabilities are interpolated from a single site  
323 peaks-over-threshold analysis of the nearest GTSM-ERA5 record location. The geographical  
324 locations of these areas are shown in Fig. 3. From the 5,975 global coastal grid cells, ESLs at  
325 851 are computed using tide gauge data, 4,555 are calculated using an RFA of GTSM-ERA5  
326 data, and 569 are calculated using GTSM-ERA5 data from the nearest record location.  
327



328 *Figure 3: This map shows the global distribution the areas in which the tide gauge RFA is used, the GTSM-ERA5 RFA is used,*  
329 *and the areas which are interpolations of single site analysis from GTSM-ERA5.*

330 Water level records are referenced to different vertical datums, so to ensure consistency,  
331 the mean over the most recent 19-year epoch is subtract from the water level record, and  
332 the timeseries is linearly detrended to the centre year of the most recent available epoch  
333 (2002-2020), resulting in 2011. Within each cluster of gauge (or model) records, the water  
334 level time series are resampled to hourly resolution and converted to mean higher high  
335 water, defined as the mean daily highest water level over a 19-year epoch, to account for  
336 differences in tidal range between record locations. In the case of records with fewer than  
337 19 years of data available the maximum continuous epoch is used instead.



338

339 Daily highest water level is determined from the hourly time series of each measured or  
340 modelled record. The time series are then declustered using a 4-day moving window of the  
341 storm to ensure event independence. This window as selected as storms that cause surge  
342 events are known to last approximately 4 days (Haigh *et al.*, 2016). The index flood  $u$ ,  
343 defined as the 98th percentile of the declustered daily highest water levels, is used as the  
344 exceedance threshold at which to normalise the water level at each record location, as  
345 follows:

$$346 \quad \text{Normalised water level} = (\text{Observed exceedance water level} - u) / u \quad (\text{eq. 1})$$

347 The normalised datasets are then aggregated and further declustered to ensure only one  
348 peak water level is retained for each regional event. This is shown in Fig. 2B for an example  
349 grid cell. Following Hosking and Wallis (1997), a statistical heterogeneity test (H) is  
350 undertaken to ensure the homogeneity of the region. If the H-score is less than 2, then the  
351 region is considered sufficiently homogenous. If the H-score is greater than 2, then the  
352 furthest water level record from the grid cell centroid is removed from the region, and the  
353 test re-run. This process is repeated until the H-score is less than 2. In a minority of cases,  
354 the heterogeneity test fails due to an anomalous record that lies within the closest 3  
355 sampling locations to the grid cell centroid. In this instance the test is rerun, except after the  
356 furthest record is removed, all the remaining records are sequentially removed and  
357 replaced, until the H-score is less than 2.

358 After the region is confirmed to be homogenous, a Generalised Pareto distribution is fitted  
359 to the aggregated, declustered, normalised regional water levels using a penalised  
360 maximum likelihood method to estimate regional extreme water levels (REWLS). This is  
361 illustrated at an example in Fig. 2C. This is repeated for the aggregated regional water levels  
362 for each 1° by 1° grid cell. While theoretically correct, applying distribution fits to real world  
363 data can sometimes give unrealistic results, particularly in the estimation of the lower  
364 frequency space. In these cases, growth curve optimisation is undertaken to ensure the  
365 output local extreme water levels are plausible in real world scenarios. To ensure  
366 consistency, an empirical threshold of 0.35 for the shape parameter is used to determine  
367 which curves will generate unrealistic extreme water levels. The empirical threshold of the



368 shape parameter is determined based on expert judgement of plausible real world  
369 maximum surge heights in the low frequency events. To correct these curves, where this  
370 threshold is exceeded, we use the shape and scale parameters of the nearest grid cell which  
371 has a shape parameter less than 0.35. In total, 34 grid cells had their shape and scale  
372 parameters adjusted, mostly concentrated in the Gulf of Mexico and Japan.

373 Local extreme water levels (LEWLs) are then estimated from the regional growth curves  
374 using the following relationship:

$$375 \quad \quad \quad LEWL = (REWL * u) + u \quad \quad \quad (\text{eq. 2})$$

376 for each coastal point along the coastline contained within the grid cell represented by the  
377 REWL. Two example LEWL curves are shown in Fig. 2E, which have been computed using  
378 different index flood values, as indicated in Fig. 2D. The index flood,  $u$ , is used to downscale  
379 the REWLs, which represent the ESL characteristics of the entire grid cell. LEWLs are output  
380 in the format of return levels for a range of exceedance probabilities. The index  $u$  is then  
381 estimated at the coastline points using an inverse distance weighting interpolation of the  $u$   
382 values for the two closest record locations, scaled by tidal range. This deviates from the  
383 methodology set out by Sweet *et al.* (2022), in which they recommend drawing  $u$  values  
384 from a linear regression of  $u$  against tidal range values from record locations across a  
385 region. We found this approach led to significant differences in LEWLs at record locations  
386 when compared to single site analysis of water level records, and hence have modified the  
387 methodology. Fig. 2D exhibits an example of the index flood for every shoreline point in an  
388 example grid cell. Tidal ranges are calculated as the difference between mean higher high  
389 water and mean lower low water. Tidal harmonics from FES2014 are used to predict mean  
390 higher high water and mean lower low water at each coastline point.

391 The last stage of the LEWL calculation involved characterisation and removal of bias in the  
392 high frequency portion of the exceedance probability curves, relative to the water level  
393 records (within which we expect the high frequency water levels to be accurately modelled).  
394 Bias is quantified based on the divergence in the 1-in-1-year return period at each tide  
395 gauge/GTSM-ERA5 location and the corresponding LEWL predictions. This bias is used as a  
396 correction term and is removed from the LEWLs. As the density of the coastline points is  
397 much greater than the density of the tide gauges/model output locations, the correction





398 term is interpolated across all coastal LEWL points based on correlation between Q99 tidal  
399 elevations computed using FES2014 at the tide gauge/GTSM-ERA5 location and  
400 neighbouring coastline points. The mean bias correction across all gauges is 8 cm.

401 Datum corrections are applied to ensure the LEWLs are correctly referenced to a vertical  
402 datum which can be used for hazard assessment applications, such as inundation modelling.  
403 Inundation models utilise digital elevation models, which typically reference a geoid as the  
404 vertical datum. The output water levels from the RFA are transformed from mean higher  
405 high water to Mean Sea Level (MSL) by adding the approximation of mean higher high water  
406 (above MSL) from the FES2014 simulations to each of the boundary condition points. The  
407 corrected MDT dataset from (Mulet *et al.*, 2021) is applied to convert water levels from MSL  
408 from the FES2014 model to the 'MSL' of a commonly used geoid, EGM08.

### 409 3.3 Validation methods

410

411 In this section we define a range of validation techniques used to address objectives 3 and 4.  
412 To validate the RFA ESLs against tide gauge records from GESLA (objective 3), a comparison  
413 is made against ESL exceedance probabilities calculated at the individual tide gauges used to  
414 inform the RFA. To quantify the degree to which the RFA approach improves the estimation  
415 of ESL exceedance probabilities compared to single site analysis (objective 4), two  
416 assessments are made.

417 Firstly, the divergence between GTSM-ERA5 RFA ESL and GTSM-ERA5 single site ESL for the  
418 entire global coastline are quantified. These are then contrasted against the differences  
419 between return levels from GTSM-ERA5 (Muis *et al.*, 2020) and COAST-RP (Dullaart *et al.*  
420 2021). GTSM-ERA5 is forced with 39 years of ERA5 data, a relatively short period when  
421 considering exceedance probabilities for rare extreme events (e.g., tropical cyclones). To  
422 overcome this data paucity, GTSM was subsequently run with STORM resulting in COAST-RP,  
423 a database containing 10,000 years of synthetic storm tracks (Bloemendaal *et al.*, 2020). The  
424 comparison can then identify regions in which the historical ESLs are poorly represented due  
425 to the limited record lengths.

426 Secondly, a leave-one-out cross validation is undertaken using GTSM-ERA5 data. Leave-one  
427 out-cross validation aims to address the common issues involved with validating statistical



428 models. One common method to validate models is split-sample validation, in which the  
429 data is split into two groups, a training set and a validation set, which are generally 70% and  
430 30% of the data respectively. The model is then trained on the larger set and validated  
431 against the smaller set. The drawbacks of this method include a highly variable validation  
432 error, due to the selection of the training and validation sets, as well as a validation error  
433 bias caused by training the model on only 70% of the available data (James *et al.*, 2013).

434 Instead of using a 70/30 split of the data, leave-one-out cross validation uses a larger  
435 proportion of the data to train the model, while validating against a smaller sub-sample, but  
436 repeats this process multiple times to generate a robust validation. In this study, 1000 grid  
437 cells which have 10 GTSM-ERA5 records used for the RFA and 3 GTSM-ERA5 record locations  
438 inside the grid cell are identified. One of the GTSM-ERA5 records from inside the grid cell is  
439 removed from the RFA process, and the REWL is calculated using the 9 remaining gauges.  
440 The LEWL is then predicted at the record location which has been left out, using the index  
441 flood,  $u$  at the record location. These LEWLs are then contrasted with a single site analysis of  
442 the water level record that was removed from the RFA. The process is then repeated for the  
443 2 other GTSM-ERA5 record locations which lie within the grid cell. This means each of the  
444 1000 models is being tested three times, against 90% of the available data, thus giving a  
445 more robust realisation of the model when trained on 100% of the data.

446

#### 447 **4. Results**

448 The results section is divided into four sub-sections. Section 4.1 presents the results of the  
449 global application of the RFA, showing both the global view of two return periods and the  
450 return levels for selected sites around the world. Section 4.2 illustrates how the RFA  
451 methodology improves the characterisation of rare extreme events using Cyclone Yasi  
452 (objective 2). In section 4.3 we validate the RFA against estimates of ESL from GESLA tide  
453 gauges (objective 3). Finally, in section 4.4 we quantify the improvements made by using an  
454 RFA approach when compared to a single site analysis of water levels (objective 4).

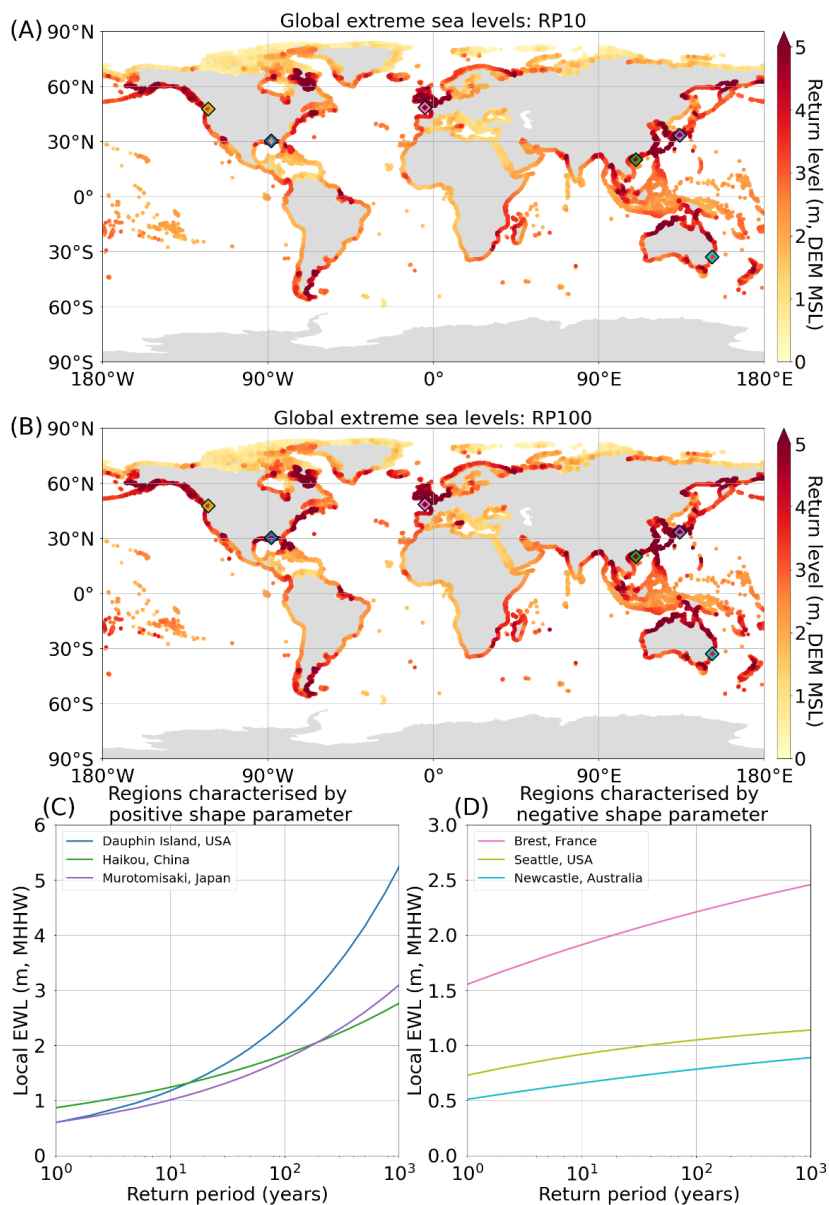
455



456 **4.1 Global application of RFA**

457 The final ESL exceedance probabilities (including wave setup) created at high resolution  
458 around the global coastline are displayed in Fig. 4, for the 1-in-10 and 1-in-100-year return  
459 periods. Both the 1-in-10 year (Fig. 4A) and 1-in-100 year (Fig. 4B) return periods show  
460 similar spatial patterns, with 1-in-100-year return periods exhibiting greater increases as  
461 expected in areas prone to tropical cyclone activity (e.g., the Gulf of Mexico, Australia,  
462 Japan, and China). ESLs are higher in regions with large tidal ranges such as the Bay of  
463 Fundy, the Patagonia Shelf, the Bristol Channel in UK, the northern coast of France, and the  
464 northwest coast of Australia. The return levels for 6 select tide gauge locations, 3 of which  
465 are characterised by a positive and 3 of which are characterised by negative shape  
466 parameter from the Generalised Pareto distribution are shown in Fig. 4C and 4D  
467 respectively, relative to mean higher high water. The locations of the 6 tide gauges are  
468 indicated in both Fig. 4A and 4B. Regions exhibiting positive shape parameters are typically  
469 prone to tropical cyclone activity and associated surge and wave events. As a result, these  
470 regions experience more significant increases in return levels at higher return periods than  
471 regions with negative shape parameters. Regions characterised by negative shape  
472 parameters have different drivers of ESL events, for instance extra-tropical storms surges or  
473 tide dominated ESLs (Sweet *et al.*, 2020).

474



475

476 *Figure 4: The final global RFA results output at approximately 1km resolution along the entire global coastline (excluding*  
 477 *Antarctica) for RP10 (A) and RP100 (B). Return levels are referenced to DEM MSL, and so represent surge, waves and tide.*  
 478 *Return levels (relative to mean higher high water) for 6 tide gauges in regions characterised by either positive or negative*  
 479 *shape parameter of the Generalised Pareto distribution are shown in panels (C) and (D) respectively. The locations of the 6*  
 480 *tide gauges are indicated by the diamonds plotted on both panels (A) and (B).*

481



482 **4.2 Tropical Cyclone Yasi**

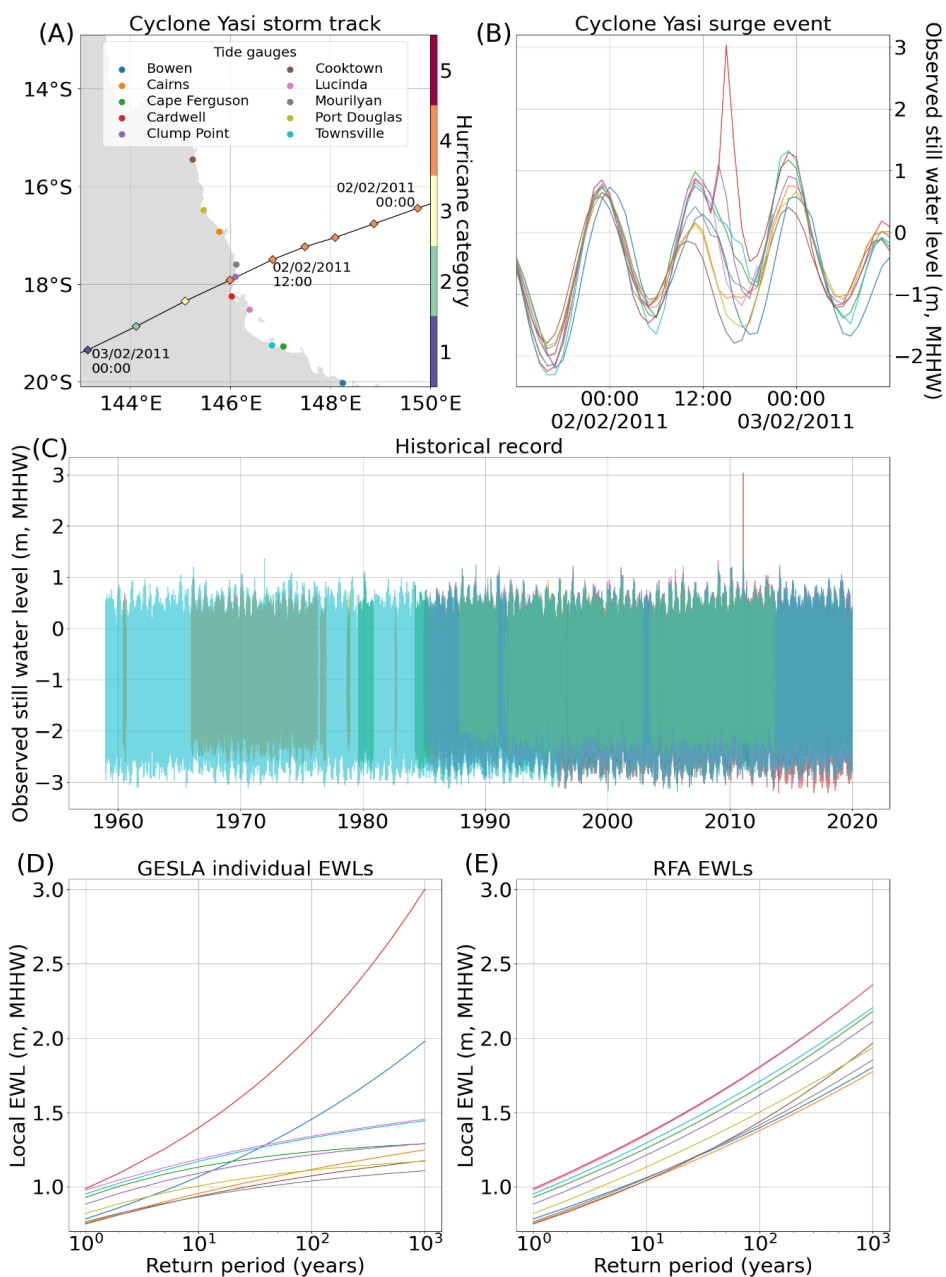
483 Our second study objective is to illustrate how the RFA methodology improves the  
484 representation of rare extreme events in the ESL exceedance probabilities, using the case  
485 study of cyclone Yasi which impacted the Australian coastline in 2011. As demonstrated in  
486 this study, one major advantage the RFA approach benefits from is its capacity to capture  
487 the extreme rare events that are typically under sampled in historical records. Cyclone Yasi  
488 made landfall on the North-eastern coast of Australia, in the Queensland region, between  
489 14:00 and 15:00 UTC on the 2nd of February 2011. It is the strongest cyclone to have  
490 impacted the region since 1918, with possible windspeeds of 285km/h and minimum record  
491 pressure centre of 929 hPa (Australia Bureau of Meteorology, 2011). When it made landfall,  
492 Yasi was a category 4 storm on the Saffir-Sampson scale. The path and strength of the storm  
493 are shown in Fig. 5A.

494 The total water levels, relative to mean higher high water, for all the tide gauges in the  
495 region are shown in Fig. 4B. Cardwell had the highest surge, and highest total water level, by  
496 a considerable margin compared to neighbouring tide gauges, receiving a surge of over 3m  
497 above mean higher high water. Clump Point also showed a definitive but less substantial  
498 surge signal, whereas the other gauges showed much smaller surge effects or even no surge  
499 at all. The historical water level records of all the gauges in the regions are included in Fig.  
500 5C. The tide gauges span different temporal ranges, and many have years which are  
501 incomplete. The longest record is at Townsville, which started in the late 1950s. Despite this  
502 record, the largest event is cyclone Yasi by over 1.5m (at Cardwell).

503 Cardwell is not unique in location. The width of the continental shelf is reasonably constant  
504 throughout this section of coastline, and while the position of the tide gauge is located  
505 towards the back of a semi-enclosed bay, any local effects due to surge (from bathymetry or  
506 coastline shape) will be accounted for by normalising the data using the index flood. Based  
507 on this historical record, no other major surge event has impacted this section of coastline  
508 since the records began. There are, however, records of other historic extreme events that  
509 predate tide gauges affecting the region. For example, Cyclone Mahina, which made landfall  
510 in Princess Charlotte Bay (approximately 100km north of Cooktown) in 1899, reportedly had  
511 a surge height approaching 10m (Needham *et al.*, 2015). The idea that this stretch of  
512 coastline is at risk of tropical cyclone generated ESLs is further supported by STORM, a



513 dataset of 10,000 years of synthetic hurricane tracks (Bloemendaal *et al.*, 2020). IBTrACS  
514 shows just eight category 4 and 5 hurricanes impacting this 700km stretch of coastline  
515 between 1980 and 2022 (shown in the Appendix Fig. A2; Knapp *et al.*, 2010). In contrast, the  
516 STORM dataset has 333 events affecting the area, producing a more continuous spread of  
517 landfall locations along the coastline. In addition, large surges are sometimes not captured  
518 in this region due to the lack of gauges in rural areas (Needham *et al.*, 2015).



519

520 *Figure 5: Tropical Cyclone Yasi: (A) The storm track of cyclone Yasi, covering a 24-hour period over the landfall event. The*  
 521 *locations of the 10 closest tide gauges along the Queensland coast are also included. Times are in UTC. (B) The observed*  
 522 *water level timeseries for the same 24-hour period at each of the 10 tide gauges in the region. Times are in UTC. (C) The*  
 523 *entire historical record of all 10 gauges in the region. (D) The return period curves of individual gauges fit with Generalised*  
 524 *Pareto distribution. (E) The return period curves at the gauge locations from the RFA.*



525 The return period curves, calculated by fitting a Generalised Pareto distribution to the  
526 peaks-over-threshold water levels at each individual tide gauge, for each of the 10 gauges in  
527 the region, are shown in Fig. 5D. As expected, Cardwell has the largest return levels and the  
528 steepest curve. All the other gauges, except Bowen, exhibit negative shape parameters,  
529 characterised by a decreasing gradient of the return period curves. In a region which is  
530 prone to tropical cyclones, this is a dangerous underestimation of the risk from cyclone  
531 induced surges. In some coastal ESL studies, ESLs are calculated at each gauge, and then  
532 interpolated along the coastline, such as in the UK (Environment Agency, 2018). In this case,  
533 that approach would lead to a gross disparity from the actual risk of storm surges to coastal  
534 communities in the area.

535 In contrast, Fig. 5E shows the return period curves estimated from the RFA at the tide gauge  
536 locations. All of the curves now have positive shape parameters, characterised by increasing  
537 gradients of the curves. The curves of Cardwell and Bowen have been reduced somewhat,  
538 while all the other curves have been increased significantly. This demonstrates the  
539 regionalisation process, by which the extreme event at Cardwell can be used to propagate  
540 the risk along the coastline to areas which have not had an extreme event on record, or  
541 have short, incomplete, or non-existent tide gauge records. This reinforces the key strengths  
542 of the RFA, namely: (1) the ability to spatially account for rare extreme events, (2) the use of  
543 short and incomplete tide gauge records to produce robust parameter fits, and (3) the  
544 ability to downscale the results into regions which aren't covered by tide gauges at all.

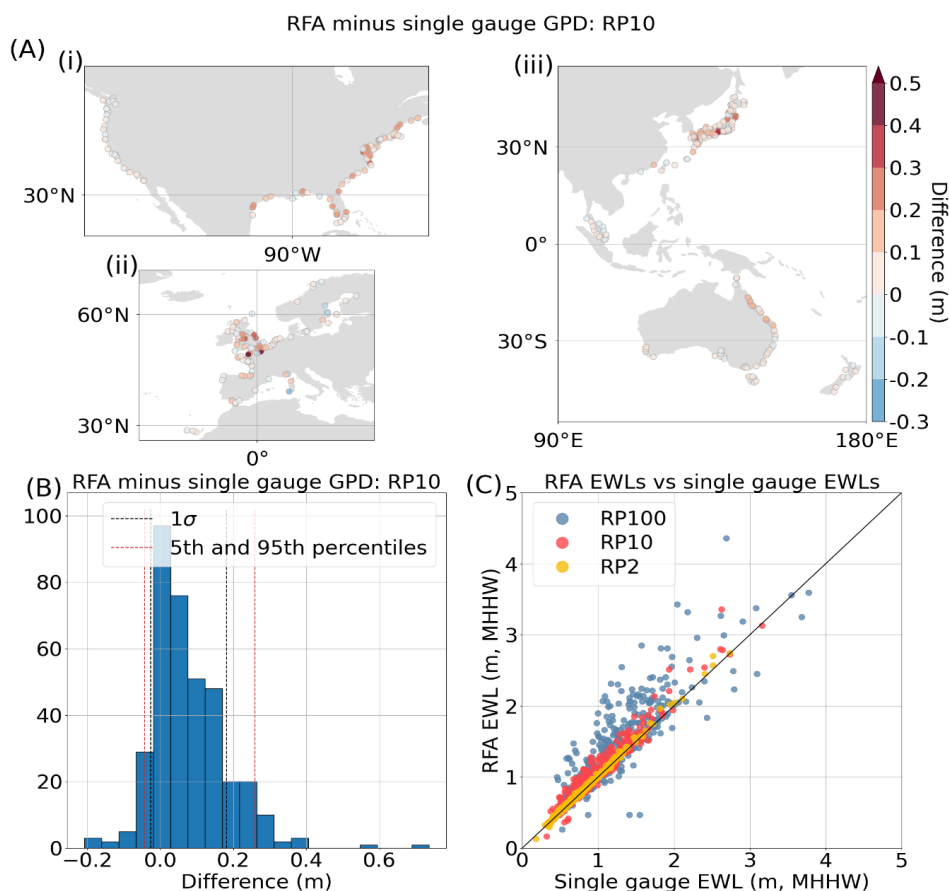
#### 545 4.3 Comparisons with GESLA

546 The third objective is to validate ESLs calculated using our RFA against those calculated  
547 directly from the measured GESLA-3 global tide gauge database. Contrasting the RFA results  
548 with ESL exceedance probabilities calculated through a Generalised Pareto distribution fit at  
549 individual tide gauges yields promising results. Fig. 6A shows the spatial distribution of the  
550 difference at the 1-in-10-year return period for Europe, the United States, and the East  
551 Pacific. In areas impacted by tropical cyclones (e.g., the Gulf of Mexico, North-Eastern Coast  
552 of Australia, and Japan) we broadly see that the RFA has increasing return levels across most  
553 gauges. Increases in the 1-in-10-year return level are also observed in areas usually  
554 associated with extra-tropical storms (e.g., Europe), suggesting gauges in these regions also  
555 suffer from under sampling of rare surge events. In all areas shown in Figure 6A, some





556 gauges show decreases in the return levels. This could be driven by either shape parameter  
 557 limiting (to prevent unrealistically large water levels), an anomalously large number of  
 558 events impacting the gauge, or due to a single anomalously large event impacting the gauge,  
 559 which is then smoothed out through the regionalisation process, as was the case in  
 560 Cardwell, Australia (Fig. 5E). The distribution of the differences at RP10 is shown in Fig. 6B  
 561 with a positive skew, detailing the 5<sup>th</sup> and 95<sup>th</sup> percentiles as -8cm and 27cm respectively.  
 562 The spread of the data increases across the three selected return periods (1-n-2, 1-in-10 and  
 563 1-in-100 year) presented in in Fig. 6C, as well as the mean bias, which increased from 2 cm  
 564 in the 1-in-2 year return level, to 21cm in the 1-in-100 year return level.



565

566 *Figure 6: Comparison of RFA water levels against extreme water levels calculated at individual gauges from GESLA by fitting*  
 567 *a Generalised Pareto distribution to peaks-over-threshold water levels. (A) The spatial distribution of the difference at RP10*  
 568 *for (i) the contiguous US, (ii) Europe, (iii) Japan, Malaysia, Australia and New Zealand, (B) a histogram of the distributions of*  
 569 *difference at RP10, including the locations of the 5<sup>th</sup> and 95<sup>th</sup> percentiles and 1 standard deviation from the mean, and (C) a*

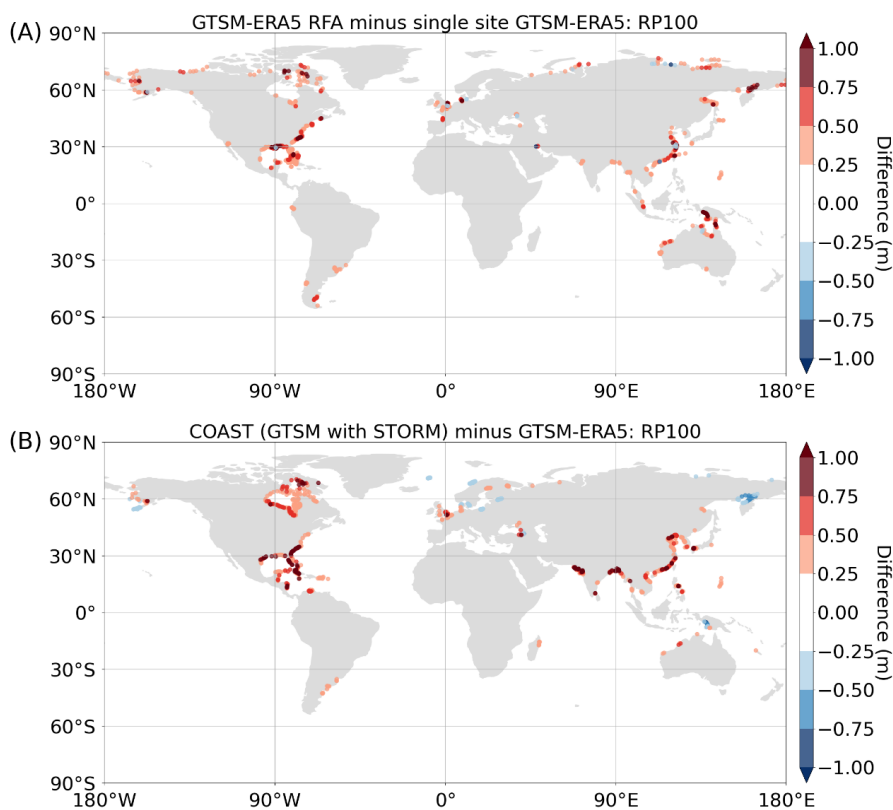


570 *scatter plot of EWLs (RP2, RP10, RP100) from the RFA and the EWLs calculated using a single site Generalised Pareto*  
571 *distribution fit. The black line indicates a 1:1 perfect fit.*

572

573 **4.4 Quantifying the improvements made by the RFA when compared to single**  
574 **site analysis**

575 The fourth objective is to quantify the improvements made to ESL exceedance probabilities  
576 by the RFA, when compared to a single site analysis. Figure 7A shows the deviation in the 1-  
577 in-100-year return period between the GTSM-ERA5 RFA carried out across the global  
578 coastline, and a single site peaks-over-threshold analysis of GTSM-ERA5 water level records.  
579 Only differences greater or less than 0.25 m and -0.25 m respectively, are plotted. There are  
580 evident increases to RFA ESLs in areas prone to tropical cyclones. The Gulf of Mexico, the  
581 East Coast of the US, Southern China, and the North-East Coast of Australia show the largest  
582 increases. Sporadic negative differences are also observed in Fig. 7A, which are driven by an  
583 over-sampling of extreme events at these record locations, and subsequent reduction in ESL  
584 exceedance probabilities by the RFA. From this we see that the RFA is capable of  
585 incorporating the influence of tropical cyclones that were not present in the historical  
586 record, but statistically could occur as indicated by the regional characteristic.



587

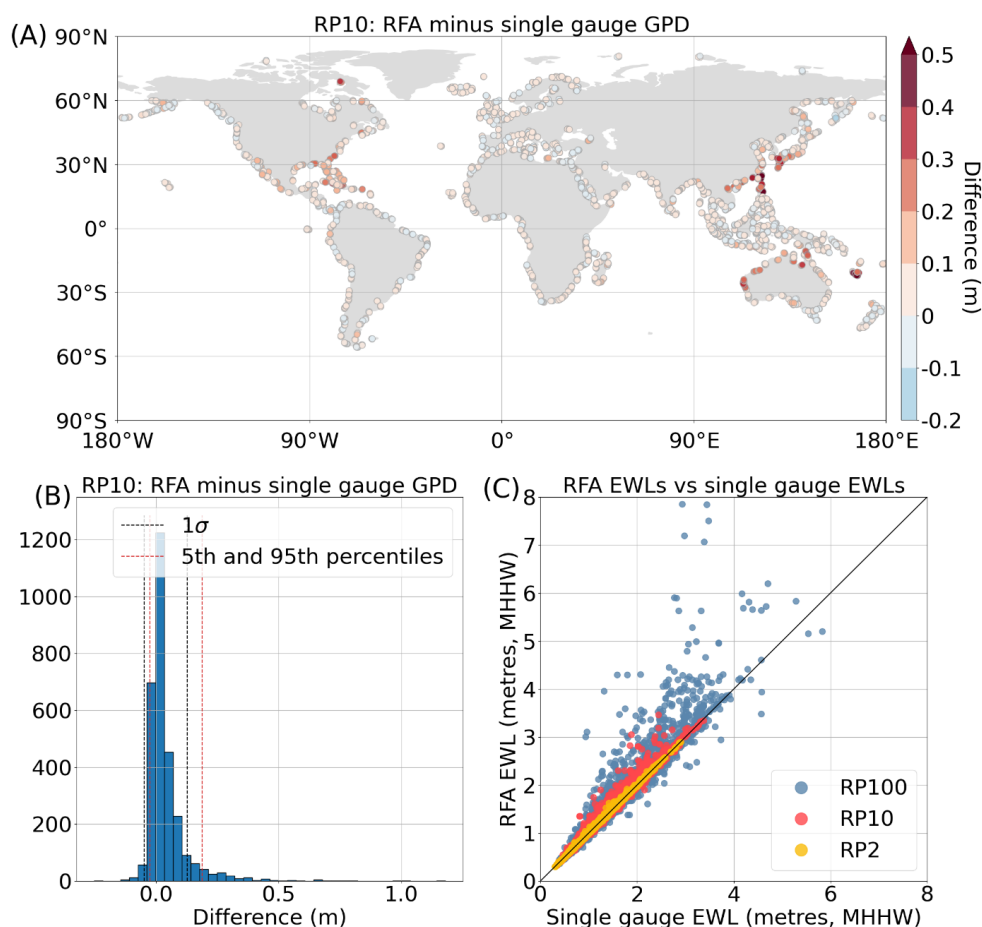
588 *Figure 7: The spatial distributions of: (A) the differences between the GTSM-ERA5 RFA 1-in-100-year return period (RP100)*  
589 *and the RP100 of single site GTSM-ERA5 data fit with a Generalised Pareto distribution to the peaks-over-threshold water*  
590 *levels; and (B) the differences in RP100 published by the COAST-RP (GTSM forced with STORM) paper (Dullaart et al., 2021)*  
591 *and RP100 published by the original GTSM paper (Muis et al., 2020). Only differences greater or less than 0.25 m and -0.25*  
592 *m, respectively, are plotted.*

593 These findings can be supported by the results shown in Fig. 7B, which shows the  
594 differences between COAST-RP and GTSM-ERA5. COAST-RP is GTSM forced with STORM  
595 (10,000 years of synthetic tropical cyclones) in areas prone to tropical cyclone activity,  
596 instead of ERA5 (Dullaart *et al.*, 2021). The areas of positive difference highlight locations  
597 where COAST-RP is greater than GTSM-ERA5, and so give an indication of the areas in which  
598 the synthetic hurricanes make landfall. These patterns are broadly similar to those of the  
599 RFA, shown in Fig. 7A. However, there are two areas which stand out for being poorly



600 characterised by the RFA, namely: the Bay of Bengal and the western Gujarat region of  
601 India. Large differences are also observed in Hudson Bay, Canada, however we suspect  
602 these discrepancies are the result of differences in the approach to modelling extra-tropical  
603 regions, as tropical cyclones do not make landfall here.

604 Figure 8 shows the results of the leave-one-out cross validation of the global coastal LEWLs.  
605 In general, the RFA tends to increase return levels due to the regionalisation process. These  
606 findings match those of (Sweet *et al.*, 2020, Sweet *et al.*, 2022) upon which our approach is  
607 based. This is evident throughout the world, with the majority of gauges exhibiting increases  
608 of less than 5 cm at the 1-in-10-year return period (Fig. 8A). The central 90th percentile  
609 band of the data for the 1-in-10-year return period ranges from -3 to 18 cm, as shown in Fig.  
610 8B. However, the spread of the data is more pronounced at the higher return periods, as  
611 shown in Fig. 8C. Some regions of the world have greater increases, in the order of 30 – 40  
612 cm for the 1-in-10 year return period. These gauges are mostly concentrated in tropical  
613 cyclone basins, namely the Caribbean, the Gulf of Mexico, Japan, China, the Philippines, plus  
614 the East and West Coasts of Australia. This demonstrates the process by which the RFA  
615 better represents extreme rare events that are typically under-sampled in the historical  
616 record. By drawing on all the events captured by gauges across the region, the RFA reveals  
617 that there is greater risk of extreme events by considering their potential occurrence in  
618 areas that, by chance, have not been previously impacted as observed in historical records.  
619 Similarly, oversampling is clearly evident at 1-in-100-year return periods, for which nearly a  
620 third of locations show decreases in ESL exceedance probabilities compared to the single  
621 site analysis. The magnitude of these decreases tend to be much smaller than the increases  
622 seen.



623

624

625 *Figure 8: The results of the leave-one-out cross validation of the RFA on GTSM-ERA5 gauges. (A) The spatial distribution of*  
 626 *difference between the leave-one-out cross validation RFA RP10 (1 in 10-year return period) and the single site Generalised*  
 627 *Pareto distribution RP10, (B) a histogram of the distribution of the differences in RP10 including the locations of the 5th and*  
 628 *95th percentiles and 1 standard deviation from the mean, and (C) a scatter plot of EWLs (RP2, RP10, and RP100)*  
 629 *predicted using the leave-one-out cross validation RFA and the EWLs calculated using a single site Generalised Pareto fit.*  
 630 *The black line indicates a 1:1 perfect fit.*

## 631 5. Discussion

632 The ESL exceedance probabilities dataset that is presented in this paper is the first global  
 633 dataset, to our knowledge, to be derived using an RFA approach, using a synthesis of  
 634 observed and modelled hindcast data. The resulting data is output at high resolution (~1  
 635 km) along the entire global coastline (excluding Antarctica), includes wave setup, and better



636 captures the coastal flood risk from tropical cyclones. This approach is notable for being  
637 computationally inexpensive compared to more traditional approaches for deriving ESL  
638 exceedance probabilities via hydrodynamic modelling.

639 As previously discussed in the introduction section, relying solely on observational records  
640 to estimate ESL exceedance probabilities can significantly bias results. To fit robust  
641 parameter estimates and obtain confident exceedance probabilities sufficient for informing  
642 flood risk managers, long term and consistent high quality observational records are needed  
643 (Coles, 2001). While some tide gauge and wave records span numerous decades, many  
644 records only cover a handful of recent decades (e.g., 10-30 years) or have significant gaps  
645 in their historical records. This often means quality data is excluded from analyses as their  
646 records are too short to produce robust parameter estimates. Furthermore, gauges are  
647 relatively sparse, especially in less populated areas and developing nations. While surges  
648 and waves typically impact large regions, peak water levels are usually only observed over  
649 smaller areas (i.e., a single bay, estuary or beach). As a result, measured records can easily  
650 miss the maximum of an extreme event, thus mischaracterising extreme water levels at the  
651 gauge. As such, rare extreme events that characterise the upmost tails of the distributions  
652 of ESLs, such as tropical cyclones, are repeatedly undersampled in the historic record, in  
653 both frequency and magnitude.

654 By using an RFA approach, we demonstrate how we have overcome these issues. The RFA  
655 can be viewed as a space-for-time approach, where long historical records (which give  
656 robust parameter estimates) are substituted for a collection of shorter records that cover a  
657 larger area. The volume of data (and subsequent extreme events) is retained, but the  
658 individual records can be much shorter. In this study, records as short as 10 years have been  
659 utilised. Furthermore, the regionalisation process works to overcome the issues with gauge  
660 density by disseminating the hazard presented by rare extreme events, as shown using the  
661 Cyclone Yasi example. From the 10 gauges in the region, the only record to have captured  
662 an historic extreme event was Cardwell, despite this section of coastline being at known risk  
663 to tropical cyclone activity. A single site analysis of tide gauge data in this region would  
664 woefully underpredict the real risk of ESLs generated by tropical cyclones.

665 Global hydrodynamic models that simulate tide and surge (e.g., GTSM) or waves have been  
666 developed to substitute observational records, especially in regions not covered by tide



667 gauges. These models have been demonstrated to represent historic extreme events to a  
668 high degree to accuracy when forced using historical observational data pertaining to the  
669 event (Yang *et al.*, 2020). However, using these models for the characterisation of  
670 exceedance probabilities is limited by the availability of long term high-quality global  
671 reanalysis data, that captures the full extent of meteorological extremes that drive large  
672 surge events. Once again, the RFA provides a solution to this problem. As demonstrated in  
673 Fig. 7, the distribution of increases to local return levels made by the RFA broadly follows  
674 the same patterns globally as the differences between COAST-RP and GTSM-ERA5. This  
675 highlights the ability of the RFA to characterise tropical cyclone hazard which is typically  
676 underrepresented as a result of short records.

677 While the RFA is capable of identifying areas of increased risk from tropical cyclone activity,  
678 it is still constrained by the training data available. This is demonstrated in Fig. 7. Two  
679 distinct areas lack increased water levels in the RFA difference plot (Fig. 7A), namely: the  
680 Bay of Bengal and Northwestern coasts of India and Pakistan. The model hindcast, GTSM-  
681 ERA5, only covers the relatively short period of 1979-2018. Consequently, the number and  
682 intensity of extreme events in GTSM-ERA5 in these regions does not accurately represent  
683 the potential hazard from tropical cyclone activity. As such, the RFA has little basis upon  
684 which to draw data from when characterising rare extreme events.

685 Coastal flood hazard mapping is usually carried out using inundation models that simulate  
686 the propagation of water over the coastal floodplain. To accurately capture the footprint of  
687 the surge on the land, inundation models require high-resolution boundary conditions at  
688 regular intervals along the coastline. The density of boundary condition points needs to be  
689 sufficient to capture local variability in ESLs along a coastline, which can be caused by  
690 bathymetric and topographic features such as narrow channels, enclosed bays, barrier  
691 island and estuaries. The spatial resolution of tide gauges, even in the areas of highest gauge  
692 density, is insufficient for direct use in inundation modelling and therefore requires some  
693 form of interpolation and/or extrapolation. Similarly, while GTSM-ERA5, is run at a  
694 reasonably high coastal resolution, publicly available data is only output at approximately  
695 50km resolution outside of Europe, and therefore does not meet the standards necessary  
696 for coastal floodplain inundation modelling. Using the RFA to downscale the regional  
697 extreme water levels allows for the possibility of implementing tide gauge data and the



698 outputs from GTSM-ERA5 as boundary conditions for subsequent inundation models. In  
699 addition, the downscaling process involves scaling the water levels by tidal range and thus  
700 enables dynamic characteristics of the surge, such as amplification at the head of estuaries,  
701 to be reproduced in the inundation models.

702 Ultimately, the future of delineating the flood hazard from tropical cyclones lies in multi-  
703 ensemble models using 100's of 1,000's of years' worth of synthetically generated storms  
704 forcing high-resolution tide-surge-wave models. However, the computational cost of  
705 running such simulations is enormous when compared to the cost of running an RFA on a  
706 relatively short hindcast record. In the same way, dynamically modelled waves are usually  
707 excluded from global simulations that consider exceedance probabilities due to the  
708 computational expense. At the same time, failing to considering the joint dependence of  
709 surge and waves can lead to an underestimation of ESL exceedance levels by up to a factor  
710 of two along 30% of the global coastline (Marcos *et al.*, 2019). This reinforces the  
711 significance of the RFA methodology in characterising global coastal flood risk.

712 Validating the RFA is nuanced, as assessing metrics compared with observed record is: (a)  
713 validating against the data used to build the RFA in the first place; and (b) not recognising  
714 the inadequacies of the tide gauge records that the RFA is attempting to mitigate. Leave-  
715 one-out cross validation highlights the strengths of the RFA, without succumbing to the  
716 shortfalls inherent in the observational record. The increased LEWLs in the regions prone to  
717 tropical cyclone activity once again demonstrates the RFA's ability to spatially disperse the  
718 hazard of low probability extreme events across a region. It is worth noting that the leave-  
719 one-out cross validation is the best possible representation of the RFA as only grid cells that  
720 use data from 10 record locations are used, so each model is trained on the maximum  
721 amount of data possible. In some areas, the number of records used can be as low as three,  
722 and so the ability for the RFA to reproduce water levels in these regions could be  
723 compromised.

724 Applying the RFA as done in this study does have its limitations. Delineating the global  
725 coastline into 1° by 1° tiles and evaluating a different RFA for each tile results in some  
726 complex areas of coastline being summarised by a single regional growth function. Examples  
727 of this are seen in Japan, where exposed coastlines of the North Coast are contained in the  
728 same tile as a sheltered bay that is open to the South Coast. A solution to this would be to





729 classify coastlines based on descriptors, as carried out by Sweet *et al.* (2020). These  
730 descriptors could include characteristics such as dominant forcing type, geographic location,  
731 and/or local coastal dynamics.

732 Going forward, the RFA framework developed in this study can be easily updated with the  
733 availability of new data. Possible next steps could also include using GTSM simulations of  
734 future climate scenarios, as well as measured wave data. To this end, a global wave dataset  
735 similar to GESLA would be instrumental in collating wave data from the numerous buoys  
736 globally.

737 In the near future, we plan to use the global exceedance probabilities derived in this paper  
738 as boundary conditions for inundation modelling of the coastal floodplain of the entire  
739 globe, using the 2D hydraulic model LISFLOOD-FP (Bates *et al.*, 2010). This presents an  
740 exciting opportunity to provide an invaluable resource that will help to better quantify  
741 global coastal flood risk.

742

## 743 6. Conclusions

744 In this paper we have demonstrated an RFA approach utilising both measured and modelled  
745 hindcast records to estimate ESL exceedance probabilities, including wave setup, at high  
746 resolution (~1 km) along the entire global coastline (with the exception of Antarctica). Our  
747 methodology is computationally inexpensive and is more effective in accurately estimating  
748 the low frequency exceedance probabilities that are associated with rare extreme events,  
749 compared to approaches that consider data from single sites. We have demonstrated, using  
750 Cyclone Yasi (2011) which impacted the Australia coast, the ability of the RFA to better  
751 characterise ESLs in regions prone to tropical cyclone activity. Furthermore, on the global  
752 scale we have exemplified how the RFA, when trained on relatively short reanalysis data,  
753 can reproduce patterns of increased water levels similar to those present in dynamic  
754 simulations of 10,000 years of synthetic hurricane tracks. The RFA methodology shown  
755 provides a promising avenue for improving our understanding of coastal flooding and  
756 enhancing our ability to prepare for and mitigate its devastating impacts. In the future, we  
757 plan to use the exceedance probabilities from this study as boundary conditions for an  
758 inundation model covering the global coastal floodplain.

759



760 7. References

761

- 762 Amadeo, K. (2019) Hurricane Harvey Facts , Damage and Costs. Retrieved from  
763 [https://www.lamar.edu/\\_files/documents/resilience-recovery/grant/recovery-and-](https://www.lamar.edu/_files/documents/resilience-recovery/grant/recovery-and-resiliency/hurric2.pdf)  
764 [resiliency/hurric2.pdf](https://www.lamar.edu/_files/documents/resilience-recovery/grant/recovery-and-resiliency/hurric2.pdf)
- 765 Andréé, E., Su, J., Larsen, M. A. D., Madsen, K. S. & Drews, M. (2021) Simulating major storm surge  
766 events in a complex coastal region. *Ocean Model.* **162**. doi:10.1016/j.ocemod.2021.101802
- 767 Andreevsky, M., Hamdi, Y., Griollet, S., Bernardara, P. & Frau, R. (2020) Regional frequency analysis of  
768 extreme storm surges using the extremogram approach. *Nat. Hazards Earth Syst. Sci.* **20**(6).  
769 doi:10.5194/nhess-20-1705-2020
- 770 Arns, A., Wahl, T., Haigh, I. D. & Jensen, J. (2015) Determining return water levels at ungauged  
771 coastal sites: a case study for northern Germany. *Ocean Dyn.* **65**(4). doi:10.1007/s10236-015-  
772 0814-1
- 773 Australia Bureau of Meteorology. (2011) Severe Tropical Cyclone Yasi. Retrieved from  
774 <http://www.bom.gov.au/cyclone/history/yasi.shtml>
- 775 Bardet, L., Duluc, C. M., Rebour, V. & L'Her, J. (2011) Regional frequency analysis of extreme storm  
776 surges along the French coast. *Nat. Hazards Earth Syst. Sci.* **11**(6). doi:10.5194/nhess-11-1627-  
777 2011
- 778 Barnard, P. L., Erikson, L. H., Foxgrover, A. C., Hart, J. A. F., Limber, P., O'Neill, A. C., Ormondt, M.  
779 van, et al. (2019) Dynamic flood modeling essential to assess the coastal impacts of climate  
780 change. *Sci. Rep.* **9**(1). doi:10.1038/s41598-019-40742-z
- 781 Bates, P. D., Horritt, M. S. & Fewtrell, T. J. (2010) A simple inertial formulation of the shallow water  
782 equations for efficient two-dimensional flood inundation modelling. *J. Hydrol.* **387**(1–2).  
783 doi:10.1016/j.jhydrol.2010.03.027
- 784 Bates, P. D., Quinn, N., Sampson, C., Smith, A., Wing, O., Sosa, J., Savage, J., et al. (2021) Combined  
785 Modeling of US Fluvial, Pluvial, and Coastal Flood Hazard Under Current and Future Climates.  
786 *Water Resour. Res.* **57**(2). doi:10.1029/2020WR028673
- 787 Bingham, R. J. & Haines, K. (2006) Mean dynamic topography: Intercomparisons and errors. *Philos.*  
788 *Trans. R. Soc. A Math. Phys. Eng. Sci.* **364**(1841). doi:10.1098/rsta.2006.1745
- 789 Bloemendaal, N., Haigh, I. D., Moel, H. de, Muis, S., Haarsma, R. J. & Aerts, J. C. J. H. (2020)  
790 Generation of a global synthetic tropical cyclone hazard dataset using STORM. *Sci. Data* **7**(1).  
791 doi:10.1038/s41597-020-0381-2
- 792 Calafat, F. M., Wahl, T., Tadesse, M. G. & Sparrow, S. N. (2022) Trends in Europe storm surge  
793 extremes match the rate of sea-level rise. *Nature* **603**(7903). doi:10.1038/s41586-022-04426-5
- 794 Caldwell, P. C., Merrifield, M. A. & Thompson, P. R. (2015) Sea level measured by tide gauges from  
795 global oceans — the Joint Archive for Sea Level holdings (NCEI Accession 0019568), Version 5.5.  
796 *NOAA Natl. Centers Environ. Inf.* (18).
- 797 Campos, R. M., Guedes Soares, C., Alves, J. H. G. M., Parente, C. E. & Guimaraes, L. G. (2019)  
798 Regional long-term extreme wave analysis using hindcast data from the South Atlantic Ocean.  
799 *Ocean Eng.* **179**. doi:10.1016/j.oceaneng.2019.03.023
- 800 Coles, S. (2001) *An Introduction to Statistical Modeling of Extreme Values*. Bristol: Springer.



- 801 Dean, R. & Walton, T. (2010) Wave Setup. In: *Handbook of Coastal and Ocean Engineering*, 1st ed.,  
802 Vol. 1–2, 1–24. World Scientific Publishing co. doi:10.1142/10353
- 803 Dullaart, J. C. M., Muis, S., Bloemendaal, N., Chertova, M. V., Couasnon, A. & Aerts, J. C. J. H. (2021)  
804 Accounting for tropical cyclones more than doubles the global population exposed to low-  
805 probability coastal flooding. *Commun. Earth Environ.* **2**(1). doi:10.1038/s43247-021-00204-9
- 806 Environment Agency. (2018) Coastal flood boundary conditions for the UK: 2018 update. Retrieved  
807 from [https://www.gov.uk/government/publications/coastal-flood-boundary-conditions-for-uk-](https://www.gov.uk/government/publications/coastal-flood-boundary-conditions-for-uk-mainland-and-islands-design-sea-levels)  
808 [mainland-and-islands-design-sea-levels](https://www.gov.uk/government/publications/coastal-flood-boundary-conditions-for-uk-mainland-and-islands-design-sea-levels)
- 809 European Space Agency. (2021) Copernicus Global Digital Elevation Model. *Open Topol.* **1**.  
810 doi:doi.org/10.5069/G9028PQB
- 811 Fanti, V., Ferreira, Ó., Kümmerer, V. & Loureiro, C. (2023) Improved estimates of extreme wave  
812 conditions in coastal areas from calibrated global reanalyses. *Commun. Earth Environ.* **4**(1).  
813 doi:10.1038/s43247-023-00819-0
- 814 Frau, R., Andreewsky, M. & Bernardara, P. (2018) The use of historical information for regional  
815 frequency analysis of extreme skew surge. *Nat. Hazards Earth Syst. Sci.* **18**(3).  
816 doi:10.5194/nhess-18-949-2018
- 817 Haigh, I D, Marcos, M., Talke, S. A., Woodworth, P. L., Hunter, J. R., Hague, B. S., Bradshaw, E., et al.  
818 (2021) GESLA Version 3: A major update to the global higher-frequency sea-level dataset.  
819 *EarthArXiv* (released), 1–34. Retrieved from <https://www.gesla.org>.
- 820 Haigh, Ivan D., MacPherson, L. R., Mason, M. S., Wijeratne, E. M. S., Pattiaratchi, C. B., Crompton, R.  
821 P. & George, S. (2014) Estimating present day extreme water level exceedance probabilities  
822 around the coastline of Australia: Tropical cyclone-induced storm surges. *Clim. Dyn.* **42**(1–2).  
823 doi:10.1007/s00382-012-1653-0
- 824 Haigh, Ivan D., Wadey, M. P., Wahl, T., Ozsoy, O., Nicholls, R. J., Brown, J. M., Horsburgh, K., et al.  
825 (2016) Spatial and temporal analysis of extreme sea level and storm surge events around the  
826 coastline of the UK. *Sci. Data.* doi:10.1038/sdata.2016.107
- 827 Hall, J. A., Gill, S., Obeysekera, J., Sweet, W., Knuuti, K. & Marburger, J. (2016) Regional Sea Level  
828 Scenarios for Coastal Risk Management : Managing the Uncertainty of Future Sea Level Change  
829 and Extreme Water Levels for Department of Defense Coastal Sites Worldwide (April), 224.  
830 Retrieved from <https://apps.dtic.mil/sti/citations/AD1013613>
- 831 Hamdi, Y., Duluc, C. M., Bardet, L. & Rebour, V. (2016) Use of the spatial extremogram to form a  
832 homogeneous region centered on a target site for the regional frequency analysis of extreme  
833 storm surges. *Int. J. Saf. Secur. Eng.* **6**(4). doi:10.2495/SAFE-V6-N4-777-781
- 834 Hersbach, H., Bell, B., Berrisford, P., Hirahara, S., Horányi, A., Muñoz-Sabater, J., Nicolas, J., et al.  
835 (2020) The ERA5 global reanalysis. *Q. J. R. Meteorol. Soc.* **146**(730), 1999–2049. John Wiley &  
836 Sons, Ltd. doi:<https://doi.org/10.1002/qj.3803>
- 837 Hosking, J. R. M. & Wallis, J. R. (1997) *Regional Frequency Analysis: An approach based on L-*  
838 *moments*, Cambridge University Press, New York. Cambridge University Press.  
839 doi:<https://doi.org/10.1017/CBO9780511529443>
- 840 India Meteorological Department. (2020) Super Cyclonic Storm Amphan over the southeast Bay of  
841 Bengal: Summary. Retrieved from  
842 [https://internal.imd.gov.in/press\\_release/20200614\\_pr\\_840.pdf](https://internal.imd.gov.in/press_release/20200614_pr_840.pdf)
- 843 Irish, J. L., Resio, D. T. & Ratcliff, J. J. (2008) The influence of storm size on hurricane surge. *J. Phys.*



- 844 *Oceanogr.* **38**(9). doi:10.1175/2008JPO3727.1
- 845 James, G., Witten, D., Hastie, T. & Tibshirani, R. (2013) *An Introduction to Statistical Learning*.  
846 Springer. doi:10.1007/9781461471387
- 847 Knapp, K. R., Kruk, M. C., Levinson, D. H., Diamond, H. J. & Neumann, C. J. (2010) The international  
848 best track archive for climate stewardship (IBTrACS). *Bull. Am. Meteorol. Soc.* **91**(3).  
849 doi:10.1175/2009BAMS2755.1
- 850 Kumar, S., Lal, P. & Kumar, A. (2021) Influence of Super Cyclone “Amphan” in the Indian  
851 Subcontinent amid COVID-19 Pandemic. *Remote Sens. Earth Syst. Sci.* **4**(1–2).  
852 doi:10.1007/s41976-021-00048-z
- 853 Liang, B., Gao, H. & Shao, Z. (2019) Characteristics of global waves based on the third-generation  
854 wave model SWAN. *Mar. Struct.* **64**. doi:10.1016/j.marstruc.2018.10.011
- 855 Lucas, C., Muraleedharan, G. & Guedes Soares, C. (2017) Regional frequency analysis of extreme  
856 waves in a coastal area. *Coast. Eng.* **126**. doi:10.1016/j.coastaleng.2017.06.002
- 857 Lyard, F. H., Allain, D. J., Cancet, M., Carrère, L. & Picot, N. (2021) FES2014 global ocean tide atlas:  
858 Design and performance. *Ocean Sci.* **17**(3), 615–649. doi:10.5194/os-17-615-2021
- 859 Marcos, M., Rohmer, J., Vousedoukas, M. I., Mentaschi, L., Cozannet, G. Le & Amores, A. (2019)  
860 Increased Extreme Coastal Water Levels Due to the Combined Action of Storm Surges and  
861 Wind Waves. *Geophys. Res. Lett.* **46**(8). doi:10.1029/2019GL082599
- 862 McGranahan, G., Balk, D. & Anderson, B. (2007) The rising tide: Assessing the risks of climate change  
863 and human settlements in low elevation coastal zones. *Environ. Urban.* **19**(1).  
864 doi:10.1177/0956247807076960
- 865 Mitchell, D., Hawker, L., Savage, J., Bingham, R., Lord, N. S., Khan, M. J. U., Bates, P., et al. (2022)  
866 Increased population exposure to Amphan-scale cyclones under future climates. *Clim. Resil.*  
867 *Sustain.* **1**(2), 1–16. doi:10.1002/cli2.36
- 868 Mori, N., Yasuda, T., Arikawa, T., Kataoka, T., Nakajo, S., Suzuki, K., Yamanaka, Y., et al. (2019) 2018  
869 Typhoon Jebi post-event survey of coastal damage in the Kansai region, Japan. *Coast. Eng. J.*  
870 **61**(3). doi:10.1080/21664250.2019.1619253
- 871 Muis, S., Apecechea, M. I., Dullaart, J., Lima Rego, J. de, Madsen, K. S., Su, J., Yan, K., et al. (2020) A  
872 High-Resolution Global Dataset of Extreme Sea Levels, Tides, and Storm Surges, Including  
873 Future Projections. *Front. Mar. Sci.* **7**(April), 1–15. doi:10.3389/fmars.2020.00263
- 874 Muis, S., Verlaan, M., Winsemius, H. C., Aerts, J. C. J. H. & Ward, P. J. (2016) A global reanalysis of  
875 storm surges and extreme sea levels. *Nat. Commun.* **7**(1), 11969. doi:10.1038/ncomms11969
- 876 Mulet, S., Rio, M. H., Etienne, H., Artana, C., Cancet, M., Dibarboure, G., Feng, H., et al. (2021) The  
877 new CNES-CLS18 global mean dynamic topography. *Ocean Sci.* **17**(3), 789–808. doi:10.5194/os-  
878 17-789-2021
- 879 Needham, H. F., Keim, B. D. & Sathiaraj, D. (2015) A review of tropical cyclone-generated storm  
880 surges: Global data sources, observations, and impacts. *Rev. Geophys.* **53**(2), 545–591.  
881 doi:10.1002/2014RG000477
- 882 Neumann, B., Vafeidis, A. T., Zimmermann, J. & Nicholls, R. J. (2015) Future coastal population  
883 growth and exposure to sea-level rise and coastal flooding - A global assessment. *PLoS One*  
884 **10**(3). doi:10.1371/journal.pone.0118571
- 885 Nicholls, R. J., Lincke, D., Hinkel, J., Brown, S., Vafeidis, A. T., Meyssignac, B., Hanson, S. E., et al.

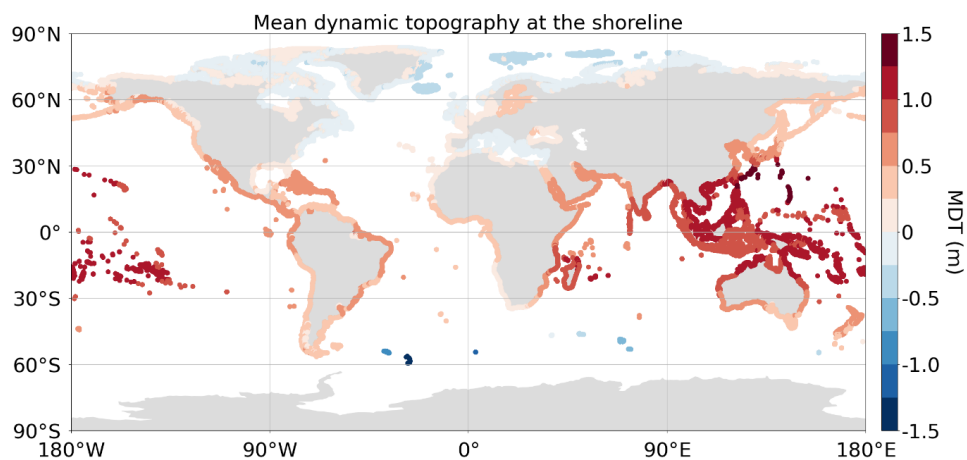


- 886 (2021) A global analysis of subsidence, relative sea-level change and coastal flood exposure.  
887 *Nat. Clim. Chang.* **11**(4). doi:10.1038/s41558-021-00993-z
- 888 Ramakrishnan, R., Remya, P. G., Mandal, A., Mohanty, P., Arayakandy, P., Mahendra, R. S. & Nair, T.  
889 M. B. (2022) Wave induced coastal flooding along the southwest coast of India during tropical  
890 cyclone Tauktae. *Sci. Rep.* **12**(1). doi:10.1038/s41598-022-24557-z
- 891 Shaji, C., Kar, S. K. & Vishal, T. (2014) Storm surge studies in the North Indian Ocean: A review. *Indian*  
892 *J. Mar. Sci.* **43**(2).
- 893 Siahsarani, A., Karami Khaniki, A., Aliakbari Bidokhti, A. A. & Azadi, M. (2021) Numerical Modeling of  
894 Tropical Cyclone-Induced Storm Surge in the Gulf of Oman Using a Storm Surge–Wave–Tide  
895 Coupled Model. *Ocean Sci. J.* **56**(3). doi:10.1007/s12601-021-00027-x
- 896 Slocum, C. J., Razin, M. N., Knaff, J. A. & Stow, J. P. (2022) Does ERA5 mark a new era for resolving  
897 the tropical cyclone environment? *J. Clim.* 1–39. doi:10.1175/jcli-d-22-0127.1
- 898 Sweet, W. V., Hamlington, B. D., Kopp, R. E., Weaver, C. P., Barnard, P. L., Bekaert, D., Brooks, W., et  
899 al. (2022) Global and Regional Sea Level Rise Scenarios for the United States. *NOAA Tech. Rep.*  
900 *NOS 01* 111 pp. Retrieved from <https://oceanservice.noaa.gov/hazards/sealevelrise/noaa-nos->
- 901 Sweet, W. V., Genz, A. S., Obeysekera, J. & Marra, J. J. (2020) A Regional Frequency Analysis of Tide  
902 Gauges to Assess Pacific Coast Flood Risk . *Front. Mar. Sci.* . Retrieved from  
903 <https://www.frontiersin.org/articles/10.3389/fmars.2020.581769>
- 904 Taherkhani, M., Vitousek, S., Barnard, P. L., Frazer, N., Anderson, T. R. & Fletcher, C. H. (2020) Sea-  
905 level rise exponentially increases coastal flood frequency. *Sci. Rep.* **10**(1). doi:10.1038/s41598-  
906 020-62188-4
- 907 Tanim, A. H. & Akter, A. (2019) Storm-surge modelling for cyclone Mora in the northern Bay of  
908 Bengal. *Proc. Inst. Civ. Eng. Marit. Eng.* **172**(3). doi:10.1680/jmaen.2019.1
- 909 Timmermans, B. W., Gommenginger, C. P., Dodet, G. & Bidlot, J. R. (2020) Global Wave Height  
910 Trends and Variability from New Multimission Satellite Altimeter Products, Reanalyses, and  
911 Wave Buoys. *Geophys. Res. Lett.* **47**(9). doi:10.1029/2019GL086880
- 912 Vanem, E. (2017) A regional extreme value analysis of ocean waves in a changing climate. *Ocean*  
913 *Eng.* **144**. doi:10.1016/j.oceaneng.2017.08.027
- 914 Vousdoukas, M. I., Voukouvalas, E., Mentaschi, L., Dottori, F., Giardino, A., Bouziotas, D., Bianchi, A.,  
915 et al. (2016) Developments in large-scale coastal flood hazard mapping. *Nat. Hazards Earth*  
916 *Syst. Sci.* **16**(8). doi:10.5194/nhess-16-1841-2016
- 917 Wang, J. & Wang, Y. (2022) Evaluation of the ERA5 Significant Wave Height against NDBC Buoy Data  
918 from 1979 to 2019. *Mar. Geod.* **45**(2). doi:10.1080/01490419.2021.2011502
- 919 Weiss, J. & Bernardara, P. (2013) Comparison of local indices for regional frequency analysis with an  
920 application to extreme skew surges. *Water Resour. Res.* **49**(5). doi:10.1002/wrcr.20225
- 921 Yang, Z., Wang, T., Castrucci, L. & Miller, I. (2020) Modeling assessment of storm surge in the Salish  
922 Sea. *Estuar. Coast. Shelf Sci.* **238**. doi:10.1016/j.ecss.2019.106552

923

## 924 8. Appendix

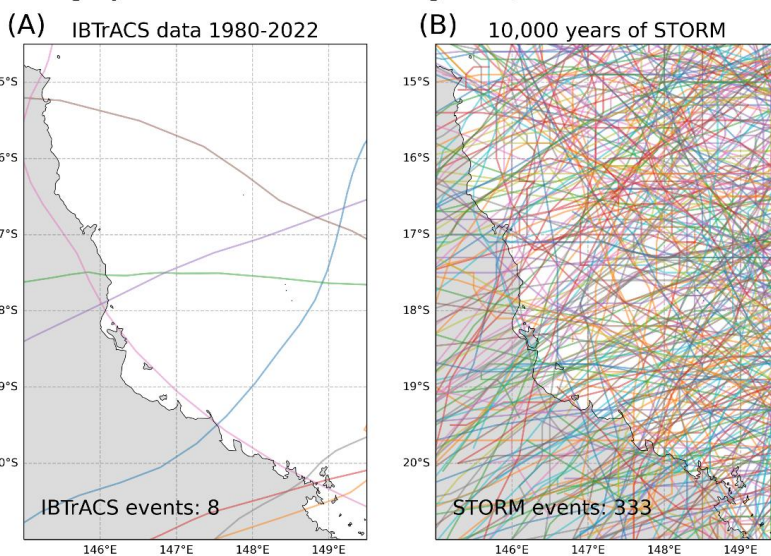
925



926

927 *Figure A1: HYBRID-CNES-CLS18-CMEMS2020 MDT dataset from Mulet et al., (2021), extracted at the shoreline for use in*  
928 *correcting the output from the RFA for future uses such as inundation modelling.*

### Category 4 and 5 hurricanes along the Queensland coastline



929

930 *Figure A2: (A) Category 4 and 5 IBTrACS hurricane impacting the Queensland coastline between 1980-2022 (Knapp et al.,*  
931 *2010) and (B) equivalent STORM events impacting the same the stretch of coastline (Bloemendaal et al., 2020).*

932

933

934

935



936 9. Code Availability

937 The Python scripts used for handling the GESLA dataset can be downloaded for:

938 <https://github.com/philiprt/GeslaDataset>

939 The Conda package (Python) used for creating the FES2014 tidal timeseries can found at:

940 <https://anaconda.org/fbriol/pyfes>

941 10. Data availability

942 GESLA tide gauge data is available at: <https://gesla787883612.wordpress.com/downloads/>

943 GTSM data is available at: <https://cds.climate.copernicus.eu/cdsapp#!/dataset/sis-water-level-change-timeseries?tab=overview>

945 ERA5 wave hindcast data is available at:

946 <https://cds.climate.copernicus.eu/cdsapp#!/dataset/reanalysis-era5-single-levels?tab=overview>

947 FES2014 tidal heights can be downloaded from:

948 <https://www.aviso.altimetry.fr/en/data/products/auxiliary-products/global-tide-fes.html>

949 HYBRID-CNES-CLS18-CMEMS2020 is available at:

950 <https://www.aviso.altimetry.fr/en/data/products/auxiliary-products/mdt/mdt-global-hybrid-cnes-cls-cmems.html>

952 Copernicus 30m DEM is found at: <https://spacedata.copernicus.eu/collections/copernicus-digital-elevation-model>

954 COAST-RP dataset is downloaded from: [https://data.4tu.nl/articles/\\_/13392314](https://data.4tu.nl/articles/_/13392314)

955 The data produced in this study is available for academic, non-commercial research only. Please  
956 contact the corresponding author for access.

957 11. Author contributions

958 T.C. was responsible for coding up the pre-processing the tide gauge and GTSM data, coding up the  
959 RFA and validating the results. N.Q. pre-processed the wave data, including fitting the copula to  
960 predict wave conditions for tide gauge records that extended beyond the hindcast period. J.G.  
961 created the coastline output points using the Copernicus DEM. I.P. worked on the evaluating the  
962 empirical shape parameter limiter. H.W. assisted in validating the output results from the RFA. S.M.  
963 supplied the GTSM dataset and W.S. provided the RFA methodology which we applied globally. I.H.  
964 and P.B. provided guidance and assistance throughout. T.C. prepared the manuscript with  
965 contributions and editing from all co-authors.

966 12. Competing Interests

967 The authors declare that they have no conflict of interest.